ADVANCED FUNCTIONAL MATERIALS
www.afm-journal.de

3D Assembly of Cryo(Bio)Printed Modular Units for Shelf-Ready Scalable Tissue Fabrication

*Zeyu Luo, Liming Lian, Thiago Stocco, Jie Guo, Xuan Mei, Ling Cai, Syed Muntazir Andrabi, Yajuan Su, Guosheng Tang, Hossein Ravanbakhsh, Wanlu Li, Mian Wang, Xiao Kuang, Carlos Ezio Garciamendez-Mijares, Di Wang, Zongliang Wang, Junlong Liao, Maobin Xie, Jingwei Xie, Heemin Kang, Anderson Oliveira Lobo, Zongke Zhou, and Yu Shrike Zhang**

The human body relies on modular assembly for realizing its functions. Here the development of a bioinspired cryo(bio)printing-based method is reported to fabricate shelf-ready, storable modular scaffolds toward scalable tissue assembly. The mechanism lies in that the cryo(bio)printed modular scaffolds are first assembled into the final hierarchy in their frozen state, which can be subsequently bonded together into an integral piece by contacting each other at the interface during the melting and photocrosslinking processes. This method not only addresses the height limitation associated with the recently developed cryo(bio)printing technology by enabling scalable tissue fabrication through modular assembly, but also allows generating tissue constructs of same or dissimilar materials to fit defects of different scales and shapes, thus providing more precision treatment. Cellular evaluations on the cryobioprinted modular hydrogels validate cell viability, spreading, and differentiation following assembly. The chick ex ovo and rat subcutaneous implantation assays further confirm the potential of direct in vivo assembly using shelf-ready cryobioprinted modular tissue constructs.

1. Introduction

The three-dimensional (3D) bioprinting technologies have enabled significant progress in tissue fabrication and regenerative medicine over the past decade.[1–4] To address some limitations of the conventional 3D bioprinting strategies such as the shelf-readiness and long-term preservation, we recently developed an enabling extrusion-based technique that we termed 3D cryobioprinting,[5,6] which combined 3D bioprinting and cryopreservation to fabricate high-fidelity cell-laden hydrogel scaffolds with simultaneous shelf-storage capacity for on-demand applications. During both the cryobioprinting and cryopreservation processes, the scaffolds are fixed in shape at low temperatures, after which they are revived and crosslinked for usage at the target time and site. Nevertheless,

Z. Luo, L. Lian, T. Stocco, J. Guo, X. Mei, L. Cai, G. Tang, H. Ravanbakhsh, W. Li, M. Wang, X. Kuang, C. E. Garciamendez-Mijares, D. Wang, Z. Wang, J. Liao, M. Xie, Y. S. Zhang
Division of Engineering in Medicine
Department of Medicine
Brigham and Women's Hospital
Harvard Medical School
Cambridge, MA 02139, USA
E-mail: yszhang@bwh.harvard.edu

Z. Luo, Z. Zhou
Department of Orthopedics
West China Hospital/West China School of Medicine
Sichuan University
Chengdu 610041, P. R. China

T. Stocco
Faculty of Medical Sciences
Unicamp – State University of Campinas
Campinas, SP 13083-877, Brazil

T. Stocco
Bioengineering Program, Scientific and Technological Institute
Brazil University
São Paulo, SP 08230-030, Brazil

S. M. Andrabi, Y. Su, J. Xie
Department of Surgery-Transplant and Mary & Dick Holland Regenerative Medicine Program
College of Medicine
University of Nebraska Medical Center
Omaha, NE 68198, USA

H. Ravanbakhsh
Department of Mechanical Engineering
McGill University
Montreal, QC H3A0C3, Canada

H. Kang
Department of Materials Science and Engineering
Korea University
Seoul 02841, Republic of Korea

H. Kang
College of Medicine
Korea University
Seoul 02841, Republic of Korea

The ORCID identification number(s) for the author(s) of this article can be found under https://doi.org/10.1002/adfm.202309173

DOI: 10.1002/adfm.202309173

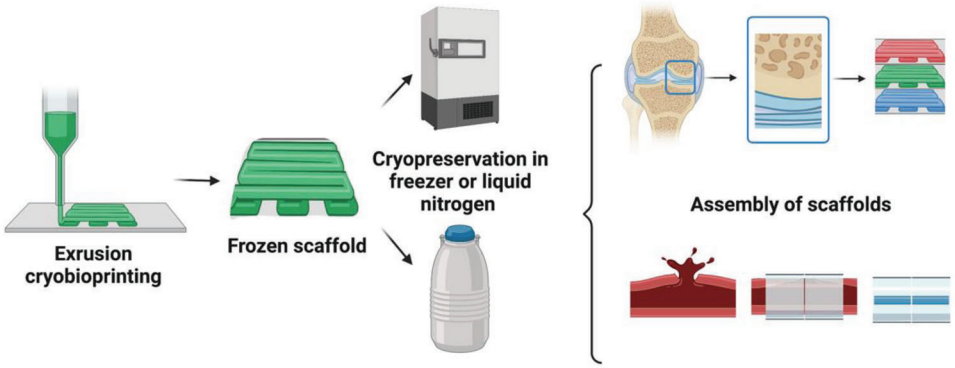

Figure 1. Schematic illustration of the concept of modular assembly of 3D-cryobioprinted shelf-storable tissue-building units for on-demand, scalable tissue fabrication. A) The cryoprotective bioink is extruded on the freezing plate to produce smaller-scale, modular scaffolds. B) The frozen scaffolds are transferred into −80 °C freezer or liquid nitrogen for shorter-term or longer-term cryopreservation, respectively, that would enable shelf-readiness of these tissue-building units. C) Upon the need for scalable tissue fabrication, the modular scaffolds are revived and assembled in vitro or in vivo. Illustrated are potential applications of the said strategy for tissue engineering, such as engineering of the cartilage-subchondral bone interface and the vasculature.

as we also identified in our initial reports,[5,6] one key limitation of the cryobioprinting method lies in the inability of producing constructs that are higher than few-mm to 1 cm, due to the heat-transfer kinetics restricted by the freezing substrate used for controlling the sub-zero temperatures during cryobioprinting.

On the other hand, assembly is a widespread phenomenon in the human body.[7] The human body is assembled hierarchically with organs from tissues that are further made of cells, which are the basic structural and functional unit of most forms of life.[8] Modular assembly in the field of bioengineering is also broadly reported,[9] such as through magnetic attraction,[10] bacterial adhesion,[11,12] interaction of phospholipid bilayer,[13] and interfacial interlocking,[14] among others. Therefore, we hypothesized that this concept might also be adaptable to our unique 3D cryobioprinting method, to allow first creation of smaller, modular tissue units that are immediately cryogenically storable, followed by assembling the desired modules together into larger-scale tissues upon on-demand usage. Each module could have same or dissimilar structures and functions as they are individually cryobioprinted, and would be conveniently bonded together by taking advantage of the room or body temperature that causes slight melting at the interfaces during the revival and photocrosslinking processes, without the need for special instrumentation.

Accordingly, we demonstrate for the first time, and optimize a technique that would further boost the capacities of our already established 3D cryobioprinting strategy,[5,6] through assembly of cryobioprinted modular constructs. As schematically briefed in **Figure 1**A, a cell-laden bioink is extruded onto a customized freezing plate. The 3D-cryobioprinted modular scaffolds of arbitrarily designed structures and functions, could be transfer into the −80 °C freezer or liquid nitrogen for cryopreservation (Figure 1B). Upon the need for subsequent usage at a desired time and location, the shelf-ready 3D-cryobioprinted modular constructs of the same or dissimilar compositions can be assembled onsite, either in vitro or in vivo, upon revival and crosslinking, in various configurations (Figure 1C). It is anticipated that our strategy of modular assembly of 3D-cryobioprinted tissue-building units for on-demand, scalable tissue fabrication may find widespread biomedical applications.

2. Results and Discussions

To optimize the conditions for the assembly of 3D-cryo(bio)printed modular scaffolds, we first compared the diffusion of GelMA molecules at different temperatures, concentrations, and time durations, respectively. Rhodamine B-conjugated GelMA was used to fabricate the scaffolds, where non-fluorescent GelMA scaffolds were adopted for assembly by photocrosslinking, for convenient visualization of the diffusion processes (**Figure 2**). To demonstrate the effect of temperature on interfacial diffusion of GelMA molecules, two pieces of frozen 7.5% (w/v for all expressions unless otherwise indicated) fluorescent/non-fluorescent GelMA blocks were assembled at different temperatures (room temperature (RT), 30, 37, and 50 °C) for 7.5 min (Figure 2A). The measured fluorescence intensity curves along the horizontal direction showed that the fluorescence intensities surrounding the interfaces of the assembled modules decreased fastest from left to right in the case of RT, where the decrease became shallower with the increase of temperature, indicating that the diffusion of GelMA was positively correlated with temperature, as expected (Figure 2B). The quantification results of the cumulative fluorescence intensities (within the non-fluorescent GelMA blocks) also revealed the same trend (Figure 2C). Nevertheless, as the temperature was further increased (60 °C and higher), the scaffolds would completely melt down within this 7.5-min timeframe after assembly and could not maintain their original shapes.

We further compared the diffusion of GelMA hydrogels at different concentrations (2.5%, 5%, 7.5%, and 10%) for 7.5 min

A. O. Lobo
Interdisciplinary Laboratory for Advanced Materials
BioMatLab
Department of Materials Engineering
Federal University of Piauí (UFPI)
Teresina, PI 64049-550, Brazil

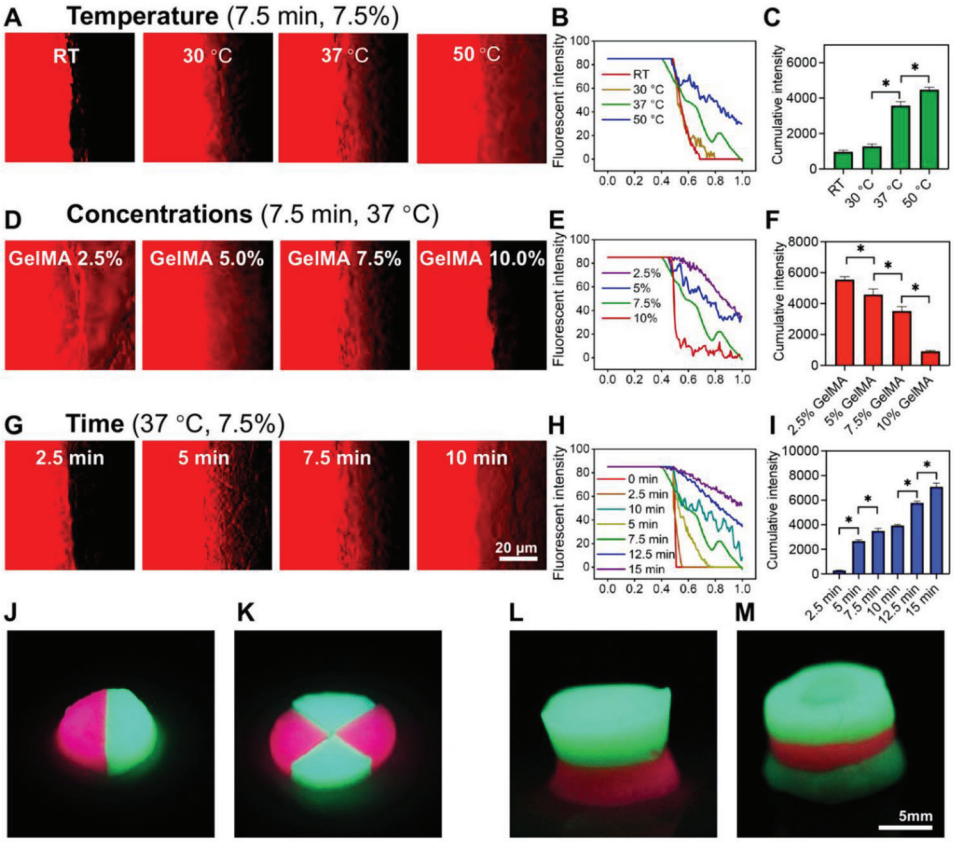

Figure 2. Diffusion characteristics of GelMA hydrogels under different conditions. Fluorescence intensity distribution A) micrographs and B) curves of 7.5% GelMA diffused at different temperatures (RT, 30, 37, and 50 °C) for 7.5 min, with C) corresponding quantification results of the intensities within the non-fluorescent GelMA blocks. Fluorescence intensity distribution D) micrographs and E) curves of different concentrations of GelMA diffused at 37 °C for 7.5 min, with F) corresponding quantification results of the intensities within the non-fluorescent GelMA blocks. Fluorescence intensity distribution G) micrographs and H) curves of 7.5% GelMA diffused at 37 °C for different times, with I) corresponding quantification results of the intensities within the non-fluorescent GelMA blocks. Exemplary modular hydrogel scaffolds assembled J,K) side-by-side and L,M) layer-by-layer. $n = 3$; $^*p < 0.05$.

after assembling the frozen pieces at 37 °C (Figure 2D). Both the fluorescence intensity curves (Figure 2E) and the quantification data (Figure 2F) demonstrated that under the same conditions, lower concentrations of GelMA diffused faster than higher concentrations, likely due to the more porous network of the lower-concentration matrices. We finally evaluated the diffusion of 7.5% GelMA after assembly at 37 °C for different times of 2.5–15 min (Figure 2G and Figure S1, Supporting Information). With the extension of duration, obviously improved diffusion could be observed (Figure 2H), where the cumulative fluorescence intensities within the non-fluorescent GelMA blocks also gradually increased (Figure 2I). Nevertheless, at 12.5 and 15 min after assembly, the scaffolds gradually melted and could not keep their original shapes despite the obvious diffusion (Figure S1, Supporting Information). According to the optimal conditions that we obtained from these sets of experiments and the previous studies we conducted,[5,6] we chose 7.5% GelMA for the subsequent experiments, where we exemplified that the 7.5% frozen modular GelMA scaffolds could be readily assembled after 10 min at 37 °C by photocrosslinking (by ultraviolet (UV) light unless otherwise noted), in either side-by-side (Figure 2J,K, Figure S2, and Movie S1, Supporting Information) or layer-by-layer (Figure 2L,M, Figure S2, and Movie S1, Supporting Information) configuration.

We also evaluated the diffusion process of 4% alginate at 37 °C after assembly by incubating in 3.0% $CaCl_2$ for different times (0–10 min) (Figure S3, Supporting Information), where it was revealed that the samples could achieve good assembly after 5 min. However, even though the samples assembled very well at 7.5 and 10 min, they melted and could not retain their original shapes (Figure S4, Supporting Information). In our previous studies, we had found that freeze-casting could produce structures with anisotropic channels, obtained via directional freezing.[6] In our current study, we used blue stain to show that the channels existed when the constructs thawed (Figure S5, Supporting Information), while the transparency observations suggested that the scaffolds remained opaque until thawing (Figure S4, Supporting Information). We further measured the diameters of the channels under the microscope, finding that the diameters of the microchannels in the scaffolds remained consistent until it was too long when the scaffolds melted completely (Figure S6, Supporting Information).

The mechanical properties are essential for target applications of the engineered tissue constructs. Accordingly, the

modularly assembled GelMA and alginate constructs were investigated for their mechanical performances with compressive and tensile testing. For better visualization, two modular scaffolds with different colors (red and green for GelMA, blue and yellow for alginate) were assembled into parallel or vertical structures (**Figure 3**). When 7.5% GelMA was assembled at 37 °C for 10 min, the compressive and tensile moduli of the resulting constructs would remain the same as the control constructs made of only single pieces of GelMA (Figure 3A,B). In addition, the assembled GelMA constructs could still reach similar compressive and tensile strengths when compared with the controls. However, as the number of assembled modules was increased to three, the tensile strength of the assembled scaffolds decreased slightly compared to that of the control group. The assembly of 4.0% alginate modular scaffolds at 37 °C for 5 min was further realized by crosslinking with 3.0% $CaCl_2$ and mechanically assessed (Figure 3C–E). Similarly, the compressive and tensile moduli as well as strengths of the assembled alginate samples, were all able to reach the same levels as the control specimens (Figure 3C,D), due to the physical crosslinking nature in this case. Moreover, similar to the GelMA group, as the number of assembly modules was increased to three, the tensile strength of the assembled scaffolds decreased slightly. Nevertheless, as shown in Figure 3E, the strain at break of the modularly assembled alginate constructs was measured at larger than 150%, slightly higher than that of the controls (Figure 3D).

To further explore the assembly performances of the 3D-cryoprinted scaffolds, we investigated the shape change of the 7.5% GelMA scaffolds over time at 37 °C (**Figure 4**A). It was observed that the 3D-cryoprinted multi-layer grids could maintain reasonable shapes for ≈5 min but suggested unwanted melting at 7.5 min. The diameters of the filaments indicated by the micrographs also revealed that there was a significant increase starting at 7.5 min (Figure 4B).

COMSOL Multiphysics was adopted to simulate heat-transfer in the cryoprinted structures. Figure 4C and Movie S2 (Supporting Information) show the simulation of heat-transfer over time during the 600 s of a cryoprinted, frozen 7.5% GelMA scaffold placed under 37 °C with a starting temperature of −20 °C. At 37 °C, the temperature of the scaffold first rapidly increased to −0.5 °C within 150 s, and the temperature increase rate became slow afterward. The reason for such an observation was because of the material's latent heat, where the construct would then go through phase-change and require additional heat to transform from solid to liquid. After 400 s, the temperature started to increase significantly again (Figure 4D). We also simulated the process of scaffold collapse based on the temperature change (Figure 4E). The cryoprinted scaffold was intact until 420 s, or 7 min, and it collapsed quickly thereafter, well-matching our experimental results in (Figure 4A,B). Hence, through experimental investigations and simulation modeling, we identified the optimal assembly time for GelMA. Our findings enabled us to determine the specific timeframe within which assembly could be accomplished most effectively, ensuring minimal melting of the material during the process.

To verify the effectiveness of larger-scale assembly of 3D-cryoprinted modular structures, we cryoprinted GelMA modules of different shapes. 3D-cryoprinted grid scaffolds (red and green) were stored in the −20 °C freezer until taken out for assembly. As shown in Figure 4F, Figure S7, and Movie S3 (Supporting Information), under our optimal conditions, these grids were seamlessly assembled vertically or laterally in various configurations to form integral, larger constructs. The assembled constructs remained mechanically intact and could be easily handled (Figure S8, Supporting Information). Similarly, the 3D-cryoprinted honeycomb module could be joined together hierarchically (Figure S9, Supporting Information). Of interest, the 3D-cryoprinted rings were cut open and then healed through reassembly and photocrosslinking, following which it could be lifted by a needle (Figure 4G and Figure S10, Supporting Information). Moreover, 3D-cryoprinted Chinese knots (red and green) could be sliced into halves and then assembled heterogeneously by photocrosslinking (Figure 4H, Figure S11, and Movie S4, Supporting Information). To further clarify the effectiveness of visible light on the modular assembly of 3D-cryobioprinted scaffolds, we used 7.5% GelMA containing tris-bipyridyl-ruthenium (II) hexahydrate (Ru) and sodium persulfate (SPS) as the photoinitiator system[15] to achieve the assembly. The results showed that the scaffolds could be well-assembled under visible light as well (Figure S12, Supporting Information). Therefore, our modular assembly method does not necessarily require the introduction of UV crosslinking potentially benefiting future translational applications.

In addition to modular assembly of 3D-cryoprinted GelMA patterns, we also applied the same method to other 3D-printable inks such as alginate, methacrylated hyaluronic acid (HAMA), and silk fibrin. Beyond the simple assemblies that we already demonstrated (Figure 3C–E), the cryoprinted modular alginate scaffolds (4.0%) were able to assemble in 3.0% $CaCl_2$ (37 °C for 3 min) into more sophisticated constructs as well (Figure S13 and Movie S5, Supporting Information). A cryoprinted alginate ring could be cut and assembled after passing through another cryoprinted ring, to form an interlocking structure following crosslinking-induced healing (Figure S13, Supporting Information). Specifically, we used a hybrid ink composed of 2.0% HAMA for optimal printability. Consistent with results from other inks, the various cryoprinted modular HAMA patterns could all be successfully assembled by UV photocrosslinking at 37 °C for 5 min (Figure S14, Supporting Information). The same observations were made when we explored the feasibility of the method to assemble cryoprinted silk fibroin (15.0%, containing Ru/SPS[15]) modules by visible-light photocrosslinking, at 37 °C for 5 min (Figure S15, Supporting Information).

In addition to the assembly of the same materials, we subsequently showed the modular assembly of dissimilar materials, i.e., building blocks cryoprinted with different ink formulations (Figure S16 and Movie S6, Supporting Information), which however, all featured the same crosslinking mechanism in each assembly. Specifically, we achieved pairwise assemblies through photocrosslinking of three types of frozen scaffolds produced by inks of 7.5% GelMA, 2.0% HAMA, and 20% poly(ethylene glycol)-diacrylate (PEGDA). Theoretically, as long as the materials can be crosslinked with each other, the modular assembly of scalable constructs would be attainable. The mechanical performances of the assembled constructs using different bioinks at 1.5 and 3 min at 37 °C were further investigated (Figure S17, Supporting Information). For the scaffolds assembled between

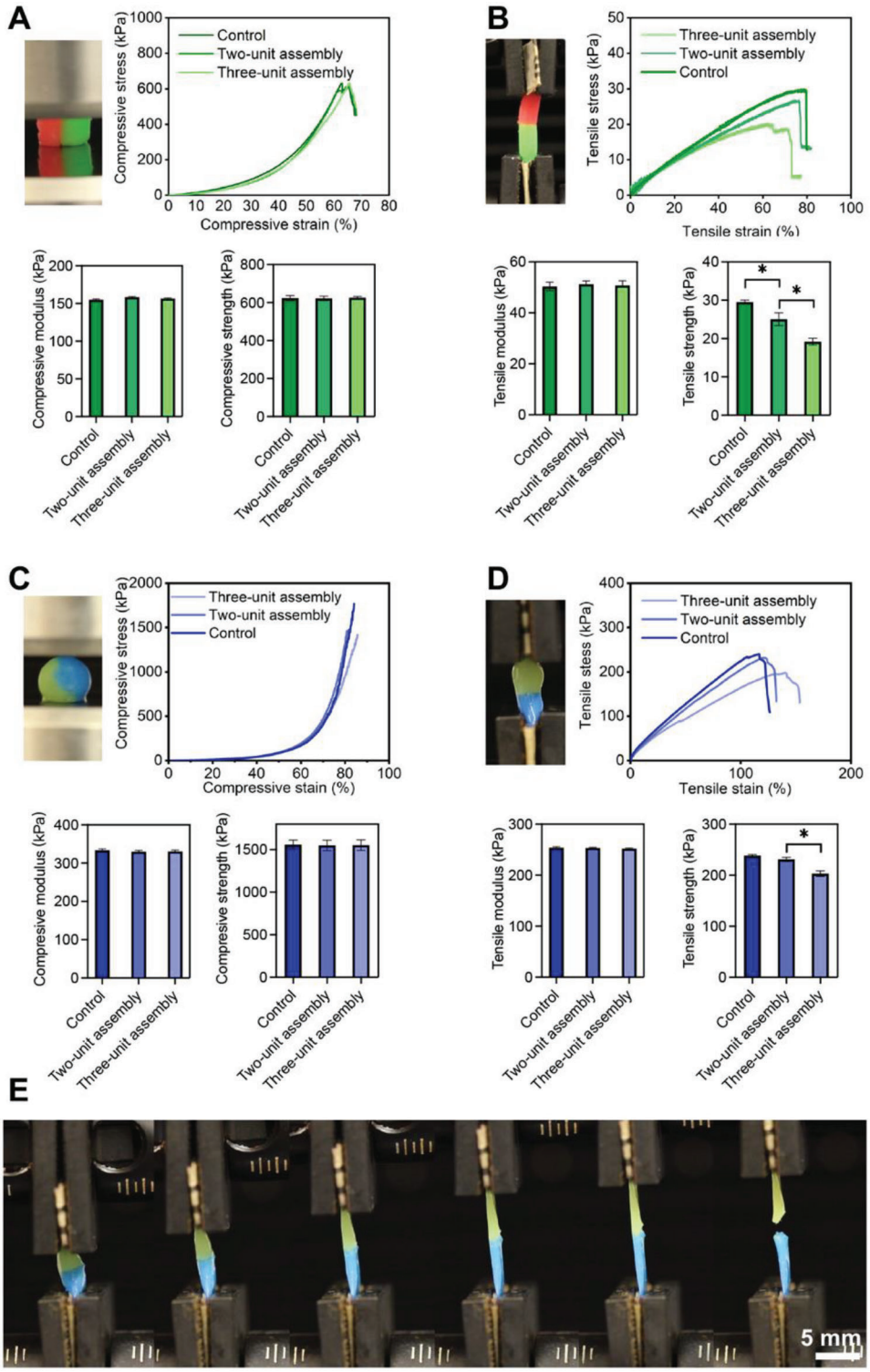

Figure 3. Mechanical characteristics of modularly assembled hydrogel constructs compared with control samples of single pieces. A) Compressive stress–strain curves and compressive moduli of the laterally assembled GelMA constructs and controls. Photograph shows the compression of an assembled construct. B) Tensile stress–strain curves and tensile moduli of the vertically assembled GelMA constructs and controls. Photograph shows the elongation of an assembled construct. C) Compressive stress–strain curves and compressive moduli of the laterally assembled alginate constructs and controls. Photograph shows the compression of an assembled construct. D) Tensile stress–strain curves and tensile moduli of the vertically assembled alginate constructs and controls. Photograph shows the elongation of an assembled construct. E) Serial photographs showing the elongation of the assembled alginate construct during the course of tensile testing until break. $n = 3$; $^*p < 0.05$.

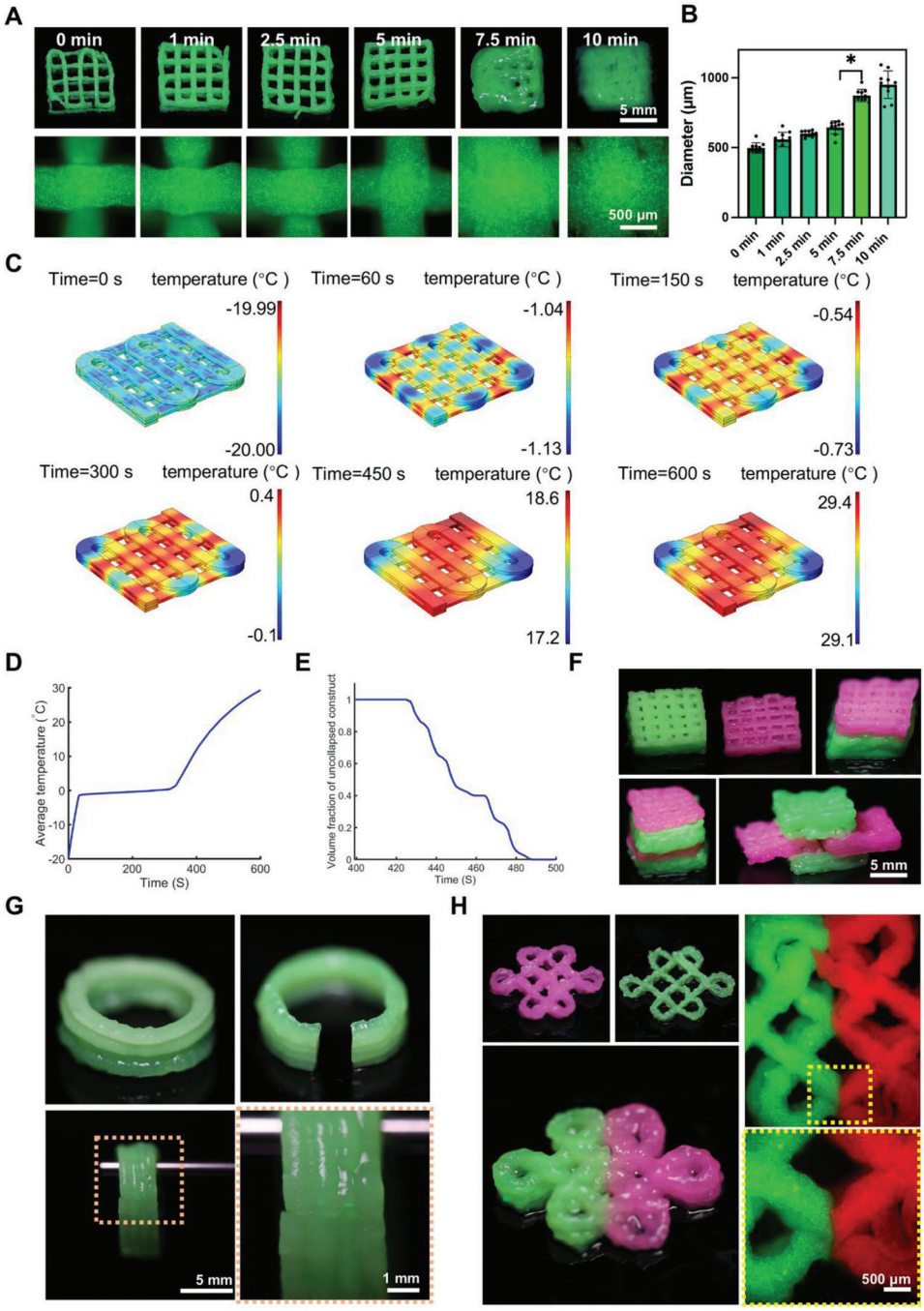

Figure 4. Experimental and simulation results on scalable assembly of 3D-cryoprinted GelMA modular patterns. A) Photographs and micrographs of the cryoprinted multi-layer 7.5% GelMA scaffold placed at 37 °C for different time points. B) Corresponding quantification results of filament diameters overtime. C) Simulated temperature change of the cryoprinted GelMA scaffold placed at 37 °C for different time points. D,E) Corresponding simulated temperature change curve and volume fraction of uncollapsed scaffold over the course of 600 s at 37 °C. F) Cryoprinted grids (red and green) and various assembled larger constructs. G) A cryoprinted ring was cut and reassembled after photocrosslinking. H) Cryoprinted Chinese knots (red and green) before and after cutting as well as photocrosslinking-induced reassembly. $n = 3$; $^*p < 0.05$.

7.5% GelMA and 2% HAMA, they reached the highest strength at 1.5 min, and the compression strain achieved ≈40% at 3 min, although the strength was decreased (Figure S17A,B, Supporting Information). For scaffolds assembled between 7.5% GelMA and 20% PEGDA, the compressive modulus reached over 300 kPa at 1.5 min, but the strength was highest at 3 min (Figure S17C,D, Supporting Information). For the scaffolds assembled with 2% HAMA and 20% PEGDA, the compressive modulus reached the highest at 3 min, which was above 150 kPa, but the strain at break was smaller at the same time duration than that at

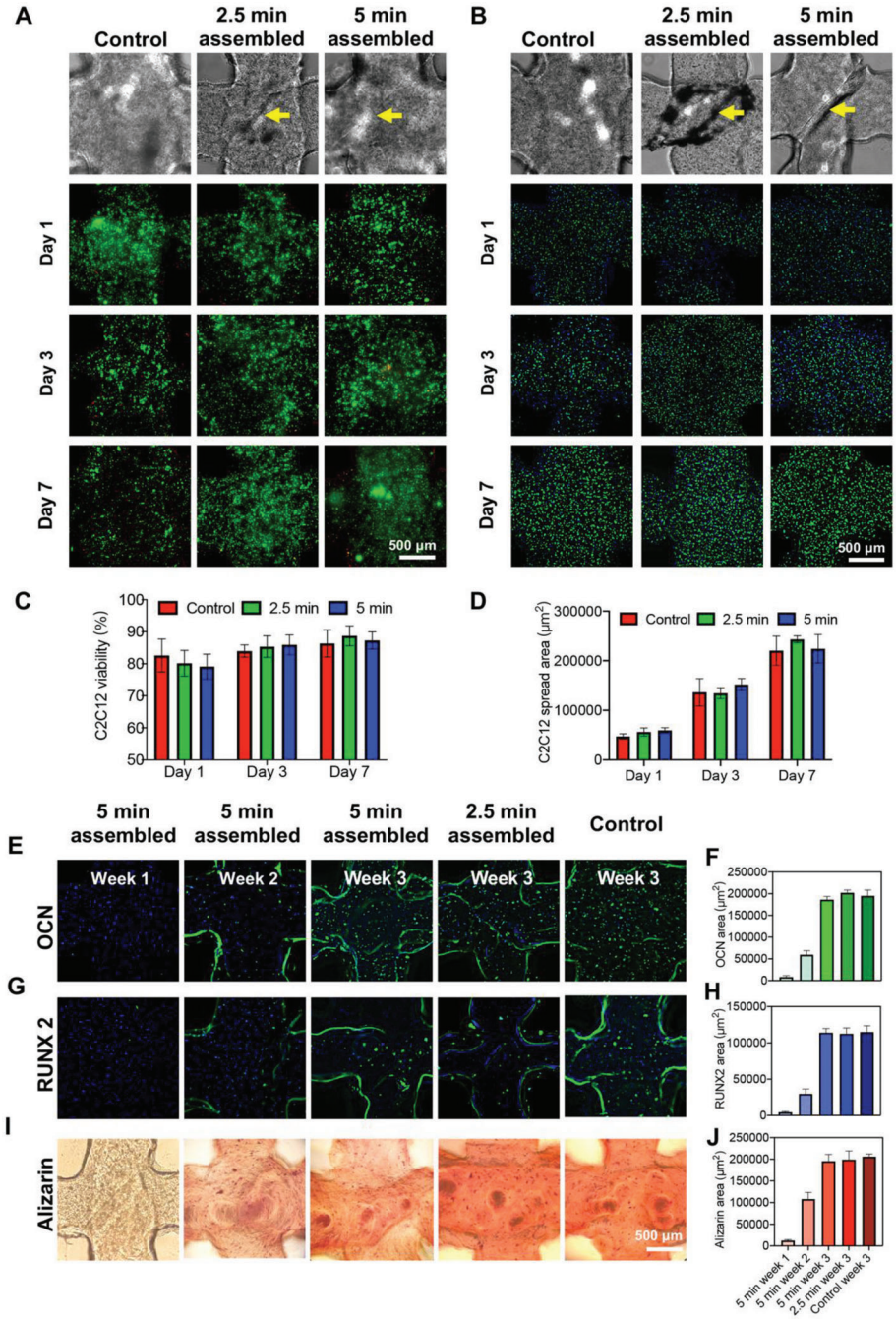

Figure 5. Viability of C2C12 myoblasts and hMSC osteogenic differentiation assay in modularly assembled 3D-cryobioprinted GelMA constructs. A) Bright-field and fluorescence micrographs showing viability of encapsulated C2C12 cells in the modularly assembled cryobioprinted constructs on Days 1, 3, and 7 of culture. Yellow arrows show the assembly interfaces. B) Corresponding quantification results of cell viability. C) Fluorescence micrographs showing C2C12 cell spreading from Day 1 to Day 7 in the modularly assembled cryobioprinted constructs. D) Corresponding quantification results of cell spreading. Osteogenic differentiation of hMSC-laden constructs: E,G) fluorescence micrographs, I) bright-field micrographs, and F,H,„J) quantitative measurements of OCN, RUNX2, and alizarin red staining results, respectively, in the modularly assembled cryobioprinted constructs on weeks 1, 2, and 3 of culture.

1.5 min (Figure S17E,F). Additional future combinations could further involve assemblies of functionally graded units of dissimilar structural properties, e.g., cryobioprinted constructs with random pores and with directionally aligned pores[5,6] to produce functionally graded tissue types.[16]

Afterward, we adopted our previously optimized cryoprotective bioink formulations for cryobioprinting studies, i.e., cryoprinting in the presence of cells.[6,17] All the samples used for assembly were first cryobioprinted and stored in the −80 °C freezer for 3 days. After the modules were taken out of the freezer,

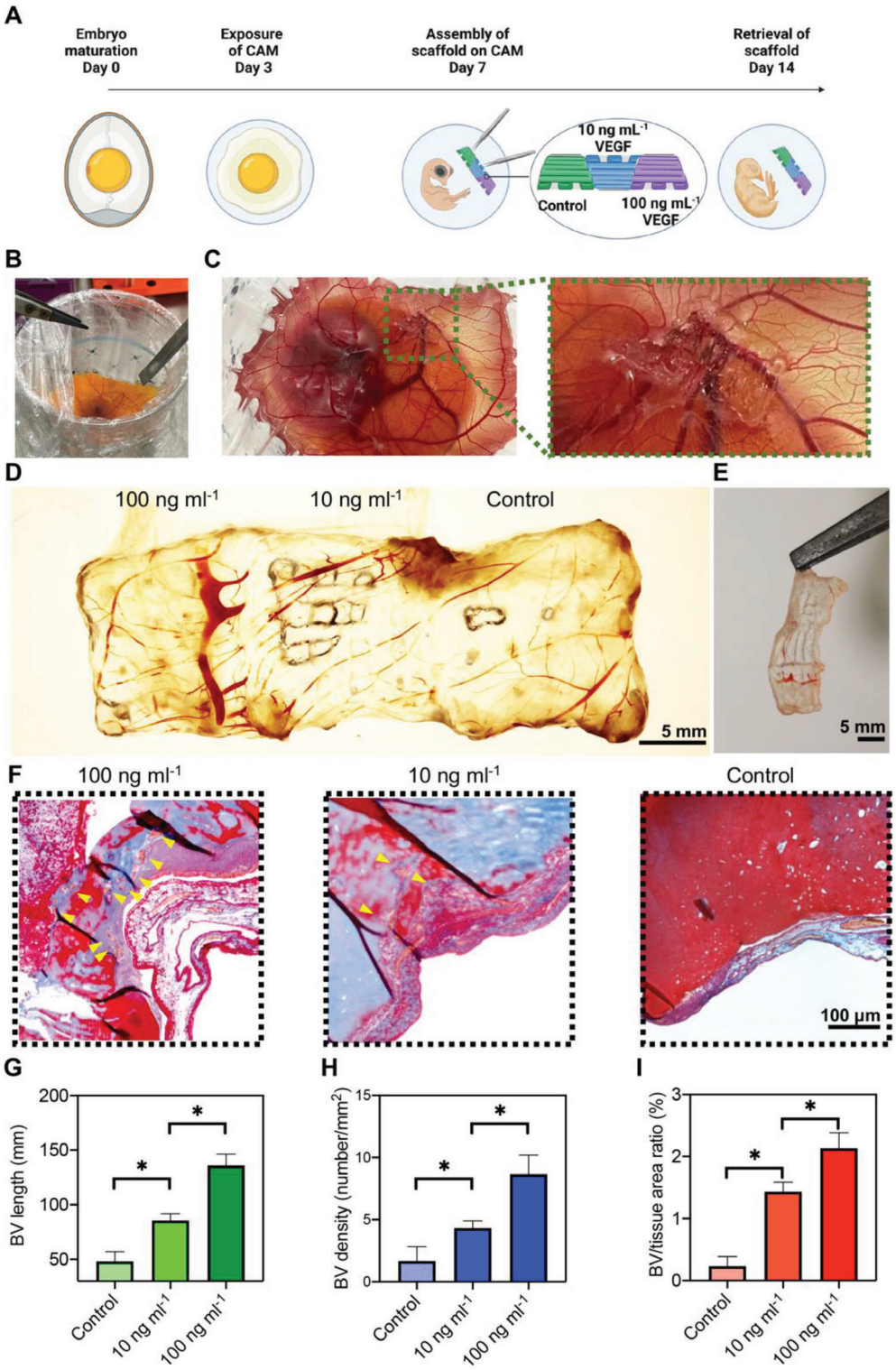

Figure 6. Evaluations of assembly of 3D-cryoprinted modules in an ex ovo CAM model. A) Schematic of evaluating the 3D cryoprinting/modular assembly approach in a chick ex ovo model. B) Photograph of the assembly process of cryoprinted VEGF-containing modules in the chick ex ovo model. C) Photographs of the assembled construct on the surface of the CAM. D) Photograph of a representative assembled sample collected after 7 days of assay. E) Photograph showing the collected module being lifted easily by a pair of tweezers. F) Masson's trichrome staining of the different modules of the collected sample, where the blood vessels are indicated by yellow arrowheads. Quantification results of neovascularization by G) BV lengths, H) BV densities, and I) of BV-to-tissue area ratios. $n = 3$; $^*p < 0.05$.

they were quickly transferred to a 37 °C incubator, and then assembled and photocrosslinked with different times (2.5 and 5.0 min), since the 3D-cryoprinted multi-layered grids would melt at 7.5 min (Figure 4A). Bright-field images clearly showed the assembly interface (yellow arrow) (**Figure 5**A). We compared C2C12 cell viability for the constructs assembled for different times. The results suggested that different assembly times had negligible effects on cell viability, and both the 2.5- and 5-min groups could reach more than 85% cell viability on the 7th day of culture (Figure 5B). We further investigated the spreading of C2C12 cells within the constructs assembled for different durations (Figure 5C). Similarly, the results of the study indicated that the assemblies for different times had no significant effect on the spreading of the embedded cells (Figure 5D). To verify whether the same cryoprotective formulation would still work with non-GelMA bioinks, we added the same cryoprotectants in 4.0% alginate and 2.0% HAMA bioinks containing NIH/3T3 fibroblasts for cryobioprinting. The cryobioprinted constructs were cryopreserved at −80 °C for 3 days and revived and cultured for 7 days. It was found that the cell viabilities in these constructs were over 80% across the culture period (Figure S18, Supporting Information), indicating that the same cryoprotective formulation that we optimized was also compatible with other types of non-GelMA bioinks.

As an example toward future clinical translation, large bone defect is common that may be caused by incidence, bone fracture, and tumor.[4,18–20] It is difficult for a single 3D-bioprinted replacement tissue to completely repair large and oftentimes irregular bone defect. Therefore, our modular assembly method provides a potential treatment option. We used human mesenchymal stem cells (hMSCs) to confirm their osteogenic functionality after assembly for different times (2.5 and 5 min) (Figure 5E,G,I). All the samples requiring assembly were placed in the −80 °C freezer for 3 days prior to assembly, the same as the cell viability test. There were three types of staining, i.e., osteocalcin (OCN), runt-related transcription factor 2 (RUNX2), and alizarin red, utilized to confirm osteogenesis of the cells. Fluorescence and bright-field micrographs captured the differentiation results of hMSCs after modular assembly at different assembly and culture times (5 min per week 1; 5 min per week 2; 5 min per week 3; 2.5 min per week 3; and control per week 3) (Figure 5E,G,I). Quantitative analyses revealed a clear increase in osteogenic differentiation from week 1 to week 3. However, osteogenic differentiation did not differ significantly for constructs assembled for different durations (control, 2.5 min, and 5 min). These findings proved the effectiveness of 3D-cryobioprinted modules to assemble and remain functional, as well as to apply to bone tissue engineering in the future.

In addition to the application to large bone defects, cartilage defects are also a widespread medical problem.[21] Our approach may be further applied to the treatment of osteochondral defects. Conceptually, by employing different types of bioinks that are specific to the local tissue microenvironments, modules of cartilage and subchondral bone, as well as their interface, could be bioprinted and assembled directly in vivo (Figure S19, Supporting Information). As a proof-of-concept demonstration, we separately bioprinted three modules with bioinks containing hMSCs labeled with different fluorescent cell tracers, showing the interfaces of the modules that were seamlessly fused together with each other through assembly (Figure S19, bottom right panels, Supporting Information).

Our modular assembly method for 3D-cryo(bio)printed patterns would potentially provide new avenues for the treatment of large skin defects as well, which may be caused by burns, accidents, and other skin diseases.[22–24] After the frozen modules were taken out from the −80 °C refrigerator, they were placed and rapidly assembled on the site of an artificially created defect in an ex vivo porcine skin obtained from the local butcher (Figure S20, Supporting Information). As with the other demonstrations, the temperature of the body may be used to quickly fuse the modules with each other prior to their photocrosslinking. In this manner, complete dressing of large and irregular skin defects becomes convenient.

The vascular system is highly complex, and there have been numerous previous studies using 3D bioprinting toward vascular tissue engineering.[25,26] Here, our approach of modular assembly was also shown to enable the fabrication of sophisticated vascular interconnectivity with simpler or smaller modules (Figure S21 and Movie S7, Supporting Information). Following assembly and photocrosslinking, it was clear that the vascular modules were tightly connected to each other showing no noticeable leakage when injecting human whole blood carrying the fluorescent dye. In addition, after injecting the human whole blood carrying the fluorescent dye at one end, all the channels were subsequently filled with fluorescence, proving that the interconnected channels still existed after the assembly. To quantitatively assess the pressure endurance of the modularly assembled vascular constructs, we conducted pressure tests. Water was injected in the assembled vascular channels until leakages were observed. Pressures were calculated from the heights of water columns to determine the stability of the vascular constructs assembled with two and three different modules with varying lumen diameters (1.6, 1.2, and 0.8 mm). Of note, the modularly assembled vascular channels with varying channel diameters exhibited good stability, as evidenced by the two-module channel could withstand pressures of up to 4.83 ± 0.28, 7.09 ± 0.50, and 10.95 ± 0.69 kPa, respectively, and the three-module channel could withstand pressures of up to 4.35 ± 0.18, 5.75 ± 0.36, and 10.82 ± 0.28 kPa, respectively (Figure S22, Supporting Information).

Similarly, we cryoprinted different modules structurally similar to the cardiovascular system, including the aorta, pulmonary artery, superior vena cava, and the heart; these modules were readily assembled to form a complete heart-like structure (Figure S23, Supporting Information). In another demonstration, we simulated the whole brain-like construct, where each of the regions with different functions, such as frontal lobe, parietal lobe, motor strip, sensory strip, Wernicke's area, temporal lobe, cerebellum, and occipital lobe could be cryoprinted separately and assembled (Figure S24, Supporting Information). While these series of demonstrations were still preliminary and lacked biological functions, they suggested the versatility of our modular assembly approach of cryobioprinted tissue-building units for future cell-laden applications.

The ex ovo chorioallantoic membrane (CAM) assay was subsequently used to evaluate the biological functions of modular assembly of 3D-cryoprinted bioactive structures. Compared to traditional animal models such as rodents, the CAM technique is a fully exposed model for visualization during the process of

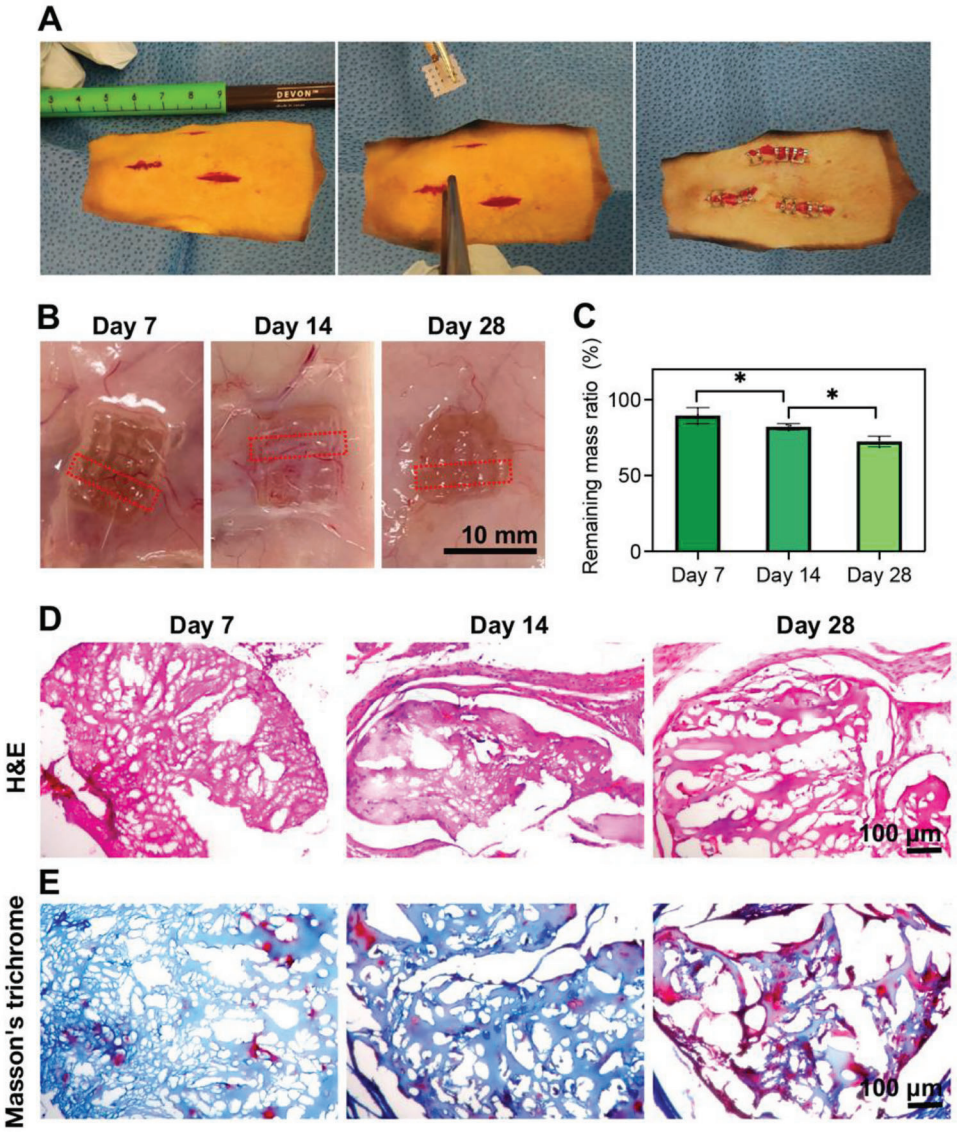

Figure 7. In vivo characterizations of the assembled 3D-cryoprinted hydrogel constructs. A) Photographs showing the subcutaneous implantation procedure of the scaffolds within rats. B) Photographs showing gross appearances of the subcutaneous implants over 4 weeks of implantation. The red dotted square in each image shows the assembly interface of the scaffold. C) Quantified degradation degrees of the scaffolds. D) H&E staining and E) Masson's trichrome staining of the scaffolds over 4 weeks of implantation. $n = 3$; $^*p < 0.05$.

modular assembly, photocrosslinking, and subsequent biological developments. We prepared 7.5% GelMA modules containing 100, 10, and 0 ng mL^{-1} of vascular endothelial growth factor (VEGF) and stored them in the −80 °C freezer for 3 days before assembly on the CAM. On the 7th day of ex ovo chorioallantoic growth, the 3D-cryoprinted modules were taken out from the −80 °C refrigerator and assembled directly on the surface of the CAM, and photocrosslinked to complete the assembly (**Figure 6**A–C). After assembly, the ex ovo CAM was cultured for another 7 days. The collected samples clearly showed that the modules had remained tightly assembled as an integral piece where they could be lifted with a pair of tweezers (Figure 6D,E), indicating the potential practicality of our method for in vivo applications. We then performed histological staining of the samples to evaluate the blood vessel (BV) lengths and densities, as well as the ratios of BV-to-tissue areas close to the surfaces of the GelMA scaffolds (Figure 6F).[6] The BV length measurements on the assembled modules revealed that the 100-ng mL^{-1} VEGF module had the longest total BVs, while the 0-ng mL^{-1} portion had the shortest total new BVs (Figure 6G). In addition, the quantified BV densities and the ratios of BV-to-tissue areas in the 100-ng mL^{-1} VEGF group were significantly higher than those in the 10-ng mL^{-1} group and the control group (Figure 6G,H). Therefore, all the results indicated that the method for 3D assembly of cryo(bio)printed modular units could not only realize the modular assembly of the scaffolds, but also maintain the differential biological functions of each individual unit.

Finally, to validate the performances of the modularly assembled scaffolds, we conducted subcutaneous implantation of pre-weighed and sterile assembled 3D-cryoprinted scaffolds (135 ± 5 mg) in rats through the incisions of 1.5 cm each, which were properly closed using wound clips (**Figure 7**A). To quantify the in vivo degradation, the implanted scaffolds were cleaned by removing any tissues on their surfaces and then dried to measure the remaining masses (Figure 7B). At 2 weeks, the hydrogels degraded by ≈20%, and at 4 weeks, the degradation was estimated at ≈30% (Figure 7C). Histologically, hematoxylin and eosin (H&E) staining and Masson's trichrome staining images depicted minimal inflammatory responses post-implantation (Figure 7D,E). These responses were characterized by the simultaneously infiltration of cells as the internal hydrogel structures progressively degraded over the 28-day period within the subcutaneous tissue pockets (Figure 7D,E).

3. Conclusions

In conclusion, we developed an enabling method to allow for modular assembly of 3D-cryo(bio)printed tissue-building units to achieve larger-scale tissue fabrication. This method can theoretically be applied to a wide variety of 3D-cryoprintable and crosslinkable biomaterial inks, where the assembled constructs would obtain mechanical properties sufficiently strong in comparison to the corresponding single-piece, non-assembled materials. The effectiveness of our method was further validated by assembling cryobioprinted cell-laden tissue structures, which showed clear viability and functional maintenance following cryogenic storage and modular assembly. We finally successfully demonstrated the proof-of-concept assembly using 3D-cryoprinted and assembled modules in a chick embryo model and a rat subcutaneous implantation model. It is believed that this method that combines bioprinting and cryostorage, yet neatly addressing its limitation of insufficient bioprinting scale due to the freezing kinetics during cryobioprinting, through modular assembly, may find widespread utility in various biomedical and biological applications in the future with further application-specific optimizations.

Supporting Information

Supporting Information is available from the Wiley Online Library or from the author.

Acknowledgements

Z.L., L.L., and T.S. contributed equally to this work. The authors acknowledge support by the Brigham Research Institute. The authors thank the NeuroTechnology Studio at Brigham and Women's Hospital for providing instrument access.

Conflict of Interest

Y.S.Z. consulted for Allevi by 3D Systems, and sits on the scientific advisory board and holds options of Xellar, neither of which however, participated in or biased the work. The other authors declare no conflict of interest.

Data Availability Statement

The data that support the findings of this study are available from the corresponding author upon reasonable request.

Keywords

3D printing, assembly, bioprinting, modular, tissue engineering, tissue model engineering

Received: August 4, 2023
Published online:

[1] R. Levato, T. Jungst, R. G. Scheuring, T. Blunk, J. Groll, J. Malda, *Adv. Mater.* **2020**, *32*, 1906423.
[2] L. Moroni, J. A. Burdick, C. Highley, S. J. Lee, Y. Morimoto, S. Takeuchi, J. J. Yoo, *Nat. Rev. Mater.* **2018**, *3*, 21.
[3] S. V. Murphy, P. De Coppi, A. Atala, *Nat. Biomed. Eng.* **2020**, *4*, 370.
[4] M. A. Heinrich, W. Liu, A. Jimenez, J. Yang, A. Akpek, X. Liu, Q. Pi, X. Mu, N. Hu, R. M. Schiffelers, J. Prakash, J. Xie, Y. S. Zhang, *Small* **2019**, *15*, 1805510.
[5] Z. Luo, G. Tang, H. Ravanbakhsh, W. Li, M. Wang, X. Kuang, C. E. Garciamendez-Mijares, L. Lian, S. Yi, J. Liao, M. Xie, J. Guo, Z. Zhou, Y. S. Zhang, *Adv. Mater.* **2022**, *34*, 2108931.
[6] H. Ravanbakhsh, Z. Luo, X. Zhang, S. Maharjan, H. S. Mirkarimi, G. Tang, C. Chávez-Madero, L. Mongeau, Y. S. Zhang, *Matter* **2021**, *5*, 573.
[7] B. K. K. Bayles, in *Proceedings of the* ASME 2012 International Mechanical Engineering Congress and Exposition. Volume 2: Biomedical and Biotechnology, ASME, Houston, Texas, November 9–15, **2012**, pp. 615–619.
[8] I. Ellinger, A. Ellinger, in *Comparative Medicine: Anatomy and Physiology* (Ed: E. Jensen-Jarolim), Springer, Vienna **2014**.
[9] Y. S. Zhang, A. Khademhosseini, *Science* **2017**, *356*, 3627.
[10] X. Kuang, S. Wu, Q. Ze, L. Yue, Y. Jin, S. M. Montgomery, F. Yang, H. J. Qi, R. Zhao, *Adv. Mater.* **2021**, *33*, 2102113.
[11] R. M. Mcbee, M. Lucht, N. Mukhitov, M. Richardson, T. Srinivasan, D. Meng, H. Chen, A. Kaufman, M. Reitman, C. Munck, D. Schaak, C. Voigt, H. H. Wang, *Nat. Mater.* **2021**, *21*, 471.
[12] B. Chen, W. Kang, J. Sun, R. Zhu, Y. Yu, A. Xia, M. Yu, M. Wang, J. Han, Y. Chen, L. Teng, Q. Tian, Y. Yu, G. Li, L. You, Z. Liu, Z. Dai, *Nat. Chem. Biol.* **2022**, *18*, 289.
[13] A. Alcinesio, I. Cazimoglu, G. R. Kimmerly, V. R. Schild, R. K. Kumar, H. Bayley, *Adv. Funct. Mater.* **2021**, *32*, 2107773.
[14] R. Subbiah, C. Hipfinger, A. Tahayeri, A. Athirasala, S. Horsophonphong, G. Thrivikraman, C. M. França, D. A. Cunha, A. Mansoorifar, A. Zahariev, J. M. Jones, P. G. Coelho, L. Witek, H. Xie, R. E. Guldberg, L. E. Bertassoni, *Adv. Mater.* **2020**, *32*, 2001736.
[15] H. Kim, B. Kang, X. Cui, S. H. Lee, K. Lee, D. W. Cho, W. Hwang, T. B. F. Woodfield, K. S. Lim, J. Jang, *Adv. Funct. Mater.* **2021**, *31*, 2011252.
[16] H. Kang, Y. Zeng, S. Varghese, *Acta Biomater.* **2018**, *78*, 365.
[17] Z. Luo, G. Tang, H. Ravanbakhsh, W. Li, M. Wang, X. Kuang, C. E. Garciamendez-Mijares, L. Lian, S. Yi, J. Liao, M. Xie, J. Guo, Z. Zhou, Y. S. Zhang, *Adv. Mater.* **2021**, *34*, 2108931.
[18] Z. Y. Luo, H. Y. Wang, D. Wang, H. Pan, F. X. Pei, Z. K. Zhou, *BMC Musculoskelet. Disord.* **2017**, *18*, 386.
[19] J. Hao, B. Bai, Z. Ci, J. Tang, G. Hu, C. Dai, M. Yu, M. Li, W. Zhang, Y. Zhang, W. Ren, Y. Hua, G. Zhou, *Bioact. Mater.* **2022**, *14*, 97.
[20] B. Xu, Z. Luo, D. Wang, Z. Huang, Z. Zhou, H. Wang, *Front. Bioeng. Biotechnol.* **2022**, *10*, 825231.
[21] L. Cui, Y. Wu, L. Cen, H. Zhou, S. Yin, G. Liu, W. Liu, Y. Cao, *Biomaterials* **2009**, *30*, 2683.

[22] T. Liu, C. Qiu, H. Lu, H. Li, S. Zhu, L. Ma, *Burns.* **2023**, *49*, 169.
[23] M. Chicco, H. T. Cheng, *J. Craniofacial Surg.* **2021**, *32*, e178.
[24] I. Osugi, K. Inagawa, S. Ebisudani, N. Hara, *Plast. Reconstr. Surg.* **2021**, *9*, e3481.
[25] X. Cao, R. Ashfaq, F. Cheng, S. Maharjan, J. Li, G. Ying, S. Hassan, H. Xiao, K. Yue, Y. S. Zhang, *Adv. Funct. Mater.* **2019**, *29*, 1807173.
[26] J. Gong, C. C. L. Schuurmans, A. M. V. Genderen, X. Cao, W. Li, F. Cheng, J. J. He, A. López, V. Huerta, J. Manríquez, R. Li, H. Li, C. Delavaux, S. Sebastian, P. E. Capendale, H. Wang, J. Xie, M. Yu, R. Masereeuw, T. Vermonden, Y. S. Zhang, *Nat. Commun.* **2020**, *11*, 1267.